Geochemical Perspectives Letters

Isotopic fractionation of neon during magma degassing

E. Núñez-Guerrero, M. Moreira, B. Scaillet

Supplementary Information

The Supplementary Information includes:

- Material and Method
- Tables S-1 to S-10
- Figures S-1 to S-4
- Supplementary Information References

Material and Method

Experimental samples:

Starting material. The initial material comprises basanitic scoria from the northeastern vent of Fasnia volcano, which erupted in January 1975 in Tenerife, Spain. This composition has previously been used for CO_2 solubility experiments (Jiménez-Mejías *et al.*, 2021) which facilitated our experiments. The chemical major element composition of the glass is shown in Table S-1. The natural sample was first crushed and powdered by using an agate mortar and acetone to prevent friction and damage to the mortar. The powdered sample was then melted at 1400 °C and 1 bar for 240 min in a platinum crucible. At the end of the experiment, the crucible was rapidly removed from the furnace and dropped into water ensuring a fast quenching. After grinding the resulting glass, this sequence was repeated once to ensure a homogeneous, anhydrous and bubble/crystal-free glass which was used as a starting material in all experiments described below.

Major elements. All glasses produced in this study were mounted in epoxy resin, polished, and analysed using a Cameca SX-Five electron microprobe at the Orléans Earth Sciences Institute (ISTO), France. Analytical conditions included an accelerating voltage of 15 kV, a beam current of 10 nA, counting times of 10 seconds per element, and a defocused beam diameter of 20 µm to minimise alkali migration. The calibration of major elements was performed using the following standards: albite (Si, Na), $TiMnO_3$ (Mn, Ti), Al_2O_3 (Al), FeO (Fe), MgO (Mg), orthoclase (K), andradite (Ca), and apatite (P). PET analyser crystals were used for elements with lower-energy emissions (K, Ti, P, and Ca), while LiF analyser crystals were employed for higher-energy emissions (Fe and Mn) (Di Carlo *et a*l., 2006). The results are presented in Table S-1.

Ne-bearing glass. A portion of the starting material was used to produce the neon-bearing glass used for the experiments. We followed the same technique as Jambon *et al.* (1986). The starting glass powder was

equilibrated in a temperature-regulated electric furnace at 1400 ^{O}C, under a constant flux of neon at 1 bar of pressure for 270 min and quenched following the same procedure as with the starting material.

To evaluate the homogeneity of the starting glass, the ^{22}Ne concentration and the isotopic composition of four chunks of glass of about 0.1-0.2 mg each were first measured using a QMS700 quadrupole-type mass spectrometer hosted at the ISTO. The sample holder where the chunks of glass were charged was baked at 100 ^{O}C and pumped for at least one day to desorb any noble gases of the glass after quenching and the inner surfaces of the laser chamber, to avoid air contamination. Once the analytical blank was low enough to start the analysis (^{22}Ne less than $2.5 \cdot 10^{-13}$ cm^3), a laser-type Ytterbium-doped fibre was used to melt the glass and release its dissolved volatiles. Each analysed piece was heated for two min to verify its complete degassing. The gas was purified and measured in the mass spectrometer. The ^{22}Ne concentration and the ^{21}Ne/^{22}Ne isotopic composition are detailed in Table S-2. The measured solubility was $3.16 \pm 0.38 \cdot 10^{-4}$ cm^{3}STP $\cdot$ g^{-1} $\cdot$ bar^{-1}.

Additionally, two pieces of the same neon-bearing glass were analysed using the newly acquired Noblesse 5F-5M noble gas mass spectrometer at ISTO Orleans, France. This instrument can resolve most isobaric interferences, including the critical ^{40}Ar^{++} interference with ^{20}Ne^{+}, which is essential to this study. Importantly, the Noblesse 5F-5M was acquired after the analyses performed with the QMS700 and HELIX-SFT mass spectrometers discussed here. As such, its data serve as subsequent confirmation of the elemental and isotopic homogeneity of the neon in the starting material.

The neon-enriched glass contains neon at abundances too high for direct analysis with either the Noblesse 5F-5M or Helix-SFT mass spectrometers. To address this, the gas was expanded into a larger volume (1 l) prior to introduction into the purification line and a volume of 0.21 cm^3 was used to introduce only a small quantity of neon into the mass spectrometer. A schematic representation of the system is provided in Figure S-1. The gas extraction followed the same protocol as with the quadrupole. The same laser type as for the QMS700 was used to bring the glass into the liquid state for two minutes, releasing the gas until *manual valve a* (Figure S-1), which corresponds to a total volume of 1100 cm^3, from which an aliquot of 0.21 cm^3 was extracted for subsequent mass spectrometer analysis. The purification protocol closely follows the procedure outlined for the Helix-SFT in the laser ablation section because the line used for the Noblesse is the same as for the Helix-SFT. Upon entering the purification line, the gas undergoes an initial stage of purification using two titanium sponge getters as it expands. In the first stage, a hot titanium getter (operating at 700 °C) absorbs gas species such as CO_2, O_2, and N_2 for five minutes. After cooling to ambient temperature, this getter continues to trap H_2 for an additional ten minutes (Stout and Gibbons, 1955). The second titanium getter further refines the gas before it is sent to cryogenic traps. At this stage, noble gases—except for neon—are captured for 15 minutes using two Cryoscan CryoSorb cold-head traps. The first trap, filled with stainless steel, adsorbs heavier noble gases (Ar, Kr, and Xe), while the second trap, made of activated charcoal, traps helium and neon and can be used to separate He from Ne. The results, summarised in Table S-3, include the ^{20}Ne/^{22}Ne and ^{21}Ne/^{22}Ne isotopic ratios derived from multiple gas aliquots (5 to 10): Table S-4 presents the run standards used throughout the analysis period. This procedure effectively minimised the blank contribution, which in this case was less than 21 %.

Capsule preparation and experimental set-up. Each capsule is set up from an $Au_{80}Pd_{20}$ tube of 2.9 mm outer diameter, 0.4 mm wall thickness and 1.5 cm length. A representative drawing of the experimental capsule is shown in Figure 4. The capsule was loaded with (1) Ne-free powdered basaltic glass, (2) silver oxalate as a source of CO_2, and (3) Ne-bearing basaltic glass for those experiments carried out with Ne. The mass of each component is given in Table S-5. The experiments were run in Internally Heated Pressure Vessels (IHPV) at ISTO, France. The experimental conditions are shown in Table S-5. All experiments were terminated by drop-

quenching (Di Carlo *et al*., 2006). A single experiment typically involved running two or more capsules simultaneously. This approach enabled us to test the same experimental conditions (P-T-duration) with varying amounts of CO_2 so as to observe its impact on vesicularity.

X-ray microtomography acquisitions

X-ray computed tomography is a non-destructive technique that allows for the precise localisation of vesicles prior to their puncturing, enabling the analysis of the gas by mass spectrometry and the characterisation of the vesicle size distribution (VSD) of the quenched glasses. The data were collected at ISTO with a Nanotom Phoenix micro-tomography system, which is equipped with a 180 kV X-ray tube with variable filament currents (40 - 170 µA) and an operating voltage of up to 120 kV.

The biggest piece of glass of every experimental capsule (sometimes several pieces at the same time) was mounted on a carbon fibre rod with a thermoplastic adhesive and then placed into the instrument to be rotated 360^{O} for the scan. Between 700 and 2000 projections were acquired with a resolution of 3 to 3.5 µm per pixel. The reconstruction of the acquired images in stacks was made via 3D with VGSudioMax. The first step is to correct for artefacts using a median filter and separating different density bands. Then we separated the portion of glass from the vesicles and the air surrounding the glass.

The microtomography images were processed using *ImageJ* to obtain the different VSDs in 2D. The *"analyse particles*" plugin was used after adjusting the threshold to obtain the surface of the glass and vesicles independently in each slice of the 2D image stack.

Vesicularity. The vesicularity of the samples was calculated using *VGStudioMax* by separating the volume of the glass from the volume occupied by the vesicles. Vesicularity is shown in Table S-9. Figure S-2 illustrates the evolution of vesicularity over time, with a representative example for each of the experiments.

Fourier-transform infrared spectroscopy (FTIR):

One or two chunks of glass for every quenched glass were doubly-polished for infrared spectroscopy analyses to thicknesses of 25-107 µm. The FTIR spectra were collected in transmission using a Nicolet 6700 FTIR spectrometer attached to an IR microscope (Nicolet Continuum) equipped with an MCT-detector at ISTO. CO_2 and H_2O contents were determined using a LEITZ DMR optical microscope equipped with an electronic X-Y stage. The absorbances of carbonate bands (≈1430 and ≈1525 cm^{-1}) and OH stretching vibration (≈3525 cm^{-1}) were determined by performing a first subtraction with the spectrum of an anhydrous decarbonated sample (the starting material in the mid-infrared (MIR) region, scaled to the same thickness, and then drawing a linear baseline below the H_2O bending and carbonate vibration bands). Typically, 128-256 scans were collected for each spectrum in the range of 1000 to 4000 cm^{-1}, with a window aperture of 40 x 40 and 20 x 20 µm and a spectral resolution of 4 cm^{-1}, collecting background on NaCl windows before each sample. The H_2O and CO_2 concentrations in the experimental glasses were determined using the Beer-Lambert law (*e.g.*, Stolper, 1982):

$$C_i = 100 \times (M_i \times A_j)/(d \times \rho \times \varepsilon_j)$$

Where C_i is the concentration of the species i in wt.%, M_i is the molecular weight of the species, A_j is the absorbance (peak height), d is the thickness of the section at each analysed point, ρ is the density of the sample (in $g \cdot l^{-1}$) and $\mathcal{E}_j$ is the absorption coefficient of band j (in $l \cdot mol^{-1} \cdot cm^{-1}$).

Despite that no water was added to the capsules, some FTIR spectra show a small amount of dissolved water generated through the reduction of Fe^{3+} of the melt during the synthesis. Thus, we decided to use the carbonate

peak of 1430 cm^{-1}, since the 1525 cm^{-1} band is slightly affected by the H_2O bending at 1630 cm^{-1}, to calculate the amount of CO_2 dissolved into the glass. Hence, the absorption coefficient considered for the 1430 cm^{-1} peak is 283 ± 8 l · mol^{-1} · cm^{-1}. The results for CO_2 and water contents are shown in Table S-6.

Laser ablation analyses:
The experimental samples were loaded into the laser cell under vacuum and baked at 100 ºC until the blank in the line was low enough ($^{22}Ne \approx 3 \cdot 10^{-13}$ cm^3STP) to start with the analysis. The drilling was done with a diode-pumped air-cooled Q-switched laser of 263 nm wavelength and 35 µm diameter, which works by repetition of power plasma pulses. This tool allows us to drill by ablation our glass chunks which are mm thick (Figure S-3) and be very precise in reaching micrometric bubbles. The pressure in the laser cell was continuously measured (in millibars) with a manometer MKS Baratron® 1 Torr full scale. When the laser ablation starts, a smooth increase in pressure happens (corresponding to the ablation of the glass). When a bubble is reached, a sharp change in the pressure is observed (Fig. S-5), and the ablation is stopped. Gas purification then starts, as explained next.

Once the gas is released from a pierced bubble the first stage of purification is performed with two Ti-sponge getters while the volume of the gas expands into the line. As explained above, during five minutes, the first hot Ti-getter (800 ºC) adsorbs chemical species like CO_2, O_2, and N_2 and then, at ambient temperature after cooling, trap H_2 for ten minutes (Stout and Gibbons, 1955). A second Ti-getter repeats the process. The noble gases, except Ne, were adsorbed for 15 minutes on activated charcoal in two cold fingers at liquid N_2 temperature. One cold finger is positioned at the end of the purification line, trapping 99 % of Ar. An additional cold finger is placed at the entrance of the mass spectrometer to reduce Ar^{++} interference before and during the Ne analysis. Before introducing Ne into a Helix-Split Flight Tube (ThermoFisher) mass spectrometer, we measured two cycles of Ne isotopes to stabilize the magnet. ^{20}Ne was measured using a mass scan instead of setting the magnet on the required field to measure ^{20}Ne, using an acceleration voltage of 4.5 kV and a trap current of 250 µA for the secondary electron multiplier (SEM) configuration.

Then Ne is introduced into the mass spectrometer. In addition to masses 20, 21, and 22, we also measured masses 40 and 44 for correcting isobaric interferences between Ar^{++} and $^{20}Ne^{+}$ and CO_2^{++} and ^{22}Ne. Fifteen cycles of measurement were done for every single vesicle, blank or standard. The acquisition software and the data processing were homemade using C# and MATLAB© respectively. The static background in the mass spectrometer was checked and estimated regularly ($^{20}Ne = 14.26 \cdot 10^{-12}$ and $^{22}Ne = 1.19 \cdot 10^{-13}$ cm^3STP). We determined the ionisation ratios $Ar^{++}/Ar^{+} = 0.03$ and $CO_2^{++}/CO_2^{+} = 0.0015$ for the Helix-SFT and corrected the partial contribution by introducing the parameters in the data processing code. The mass discrimination of the mass spectrometer is determined by averaging the standards measured over the course of the analysis of the vesicles. The standard used comes from the dilution of a volume of "one pipette" (0.1 cm^3) of atmospheric air in a reservoir of 2 l. The uncertainty in the mass discrimination is represented by the standard deviation of these standards (Table S-7). The Ne blank contribution was between 3 and 20 % except for V_7 in sample *ESFa-3B-240min* for which it was 30 %. After ablating the matrix for 10 min the matrix blank contributed to 70 %. Therefore, the correction was done directly using the line blank, since the matrix contribution can be considered negligible. Uncertainties on the isotopic ratios in the samples are derived from the propagation of the measured uncertainty, the blank correction, and the mass discrimination correction. The results of the vesicle analyses are shown in Table S-8.

Calculations:
Maximum mass fractionation factor (MFF_{Ne}). The maximum fractionation factor, was calculated using Graham's law, resulting in values of $^{20}Ne/^{22}Ne = 10.28$ and $^{21}Ne/^{22}Ne = 0.0297$. These were determined as $^{20}Ne/^{22}Ne_{Air} \cdot (m_{22}/m_{20})^{1/2}$ and $^{21}Ne/^{22}Ne_{Air} \cdot (m_{22}/m_{21})^{1/2}$ respectively.

To study the relationship between CO_2 diffusion in the melt, the displacement of bubbles along the capsule and the average growth of vesicles in the magma before quenching (Fig. 1), we calculate the following parameters.

Bubble radius growth (G_r). The growth rate of the bubbles, G_0, can provide useful information about the experimental samples. This parameter is independent of bubble size and gives information about the residence time of the bubbles in the magma, τ. Watson *et al.* (1982) calculated this value for basaltic melts using the diffusivity laws for dissolved CO_2, but Sarda and Graham (1990) observed that this value is significantly influenced by the initial CO_2 content of the magma, which is currently unknown. Consequently, the value of G_0 can vary by several orders of magnitude. In our experiments, the initial CO_2 content is known. The formula of τ, was deconvolved in order to calculate *Gr* in our experimental samples, and τ was fixed at 1800 minutes which is the time at which the run product glasses showed no more vesicles (sample *EN-E3*).

$$G_r = [1 / (\tau \times (-a))] \times time_{exp}$$

Where a is the slope of the vesicle size distribution (VSD) trend of each sample in cm and $time_{exp}$ is the time that the experiments run. These parameters, obtained by the 2D-image scan analyses are reported in Table S-9).

CO_2 diffusion in the melt (D_{CO2}). The predominant C-bearing species in basaltic melts is CO_3^{2-} (Zhang *et al.*, 2007). Because of the similarity in atomic size and mass to Ar, CO_2 diffusion is approximately the same as the chemical diffusivity of Ar in silicate melts (Zhang and Xu, 1995; Behrens and Zhang, 2001; Nowak *et al.*, 2004; Zhang *et al.*, 2007), and is described as:

$$Ln\, D_{melt} = -13.99 - (17367 + 1.9448 \times P) / T + [(855.2 + 0.2712 \times P) \times Cw] / T$$

$$D_{CO2} = D_{melt} \times time_{exp}$$

Where D_{melt} is CO_2 diffusivity in $m^2\ s^{-1}$, P is the pressure in MPa, T is the temperature in Kelvins, and Cw is the weight per cent of H_2O.

Bubble displacement (B_d). The bubble ascent rate, v_b was calculated using Stokes' Law, which describes the motion of a spherical particle through a viscous fluid.

$$v_b = -2/9 \times \left(r^2 \times g \times (\rho_b - \rho_L)\right) / \eta$$

Where r is the mean radius of the vesicles in meters, g is the gravity in $m \cdot s^{-1}$, ρ_b and ρ_L are the densities of the bubble (from Bottinga and Richet (1981) for the conditions of the experiment and the liquid respectively in $kg \cdot m^{-3}$, and η is the viscosity of the magma in $Pa \cdot s^{-1}$, calculated for each experiment using the amount of dissolved water and the experimental pressure, following the method of Giordano *et al.* (2008). The average distance of bubbles displacement during each experiment is given by:

$$B_d = v_b \times time_{exp}$$

The results are shown in Table S-10 and plotted in Figure 1. The parameters needed for the calculations can be found in Tables S-6 and S-9. In addition, the evolution of vesicularity in 3D over time is shown in Figure S-2.

Supplementary Tables

Table S-1 To ensure consistency with the data of the natural sample published by Jiménez-Mejías *et al.* (2021) (Basanite FAS*) the composition of the starting glass and the Ne-bearing glass were normalized to 100 % anhydrous (**). The sum of oxides (original totals ***) was as high as 99 %. All Fe is reported as FeO, and the standard deviation. Oxide concentrations (wt. %) measured by electron microprobe analysis at Orléans Earth Sciences Institute, France (ISTO).

	Basanite FAS*	Starting mat. **	Ne-bearing glass**	Starting mat. ***	Ne-bearing glass***
SiO_2	45.08 ± 0.14	44.86 ± 0.23	45.47 ± 0.15	44.27 ± 0.33	44.95 ± 0.28
TiO_2	3.82 ± 0.13	3.70 ± 0.18	3.78 ± 0.14	3.65 ± 0.16	3.74 ± 0.14
Al_2O_3	14.45 ± 0.17	14.87 ± 0.17	14.94 ± 0.17	14.67 ± 0.17	14.77 ± 0.12
FeO*	12.51 ± 0.27	12.39 ± 0.24	11.49 ± 0.43	12.22 ± 0.26	11.36 ± 0.48
MnO	0.28 ± 0.05	0.17 ± 0.07	0.11 ± 0.06	0.17 ± 0.07	0.11 ± 0.06
MgO	7.15 ± 0.22	7.80 ± 0.05	7.8 ± 0.11	7.69 ± 0.04	7.71 ± 0.10
CaO	10.82 ± 0.17	10.38 ± 0.10	10.43 ± 0.16	10.24 ± 0.12	10.31 ± 0.11
Na_2O	3.6 ± 0.10	3.63 ± 0.07	3.77 ± 0.08	3.59 ± 0.08	3.73 ± 0.06
K_2O	1.57 ± 0.07	1.47 ± 0.15	1.49 ± 0.04	1.45 ± 0.15	1.47 ± 0.05
P_2O_5	0.71 ± 0.07	0.73 ± 0.09	0.71 ± 0.05	0.72 ± 0.08	0.71 ± 0.05
$Na_2O + K_2O$	5.17	5.10	5.26	5.03	5.20
Total	100	100	100	98.67	98.85

Table S-2 ^{22}Ne abundances (in cm^3 STP/g) and $^{21}Ne/^{22}Ne$ ratio obtained with the quadrupole mass spectrometer for the Ne-bearing glass chunks analysed for checking homogeneity. The glass was free of vesicles and melted for 2 min under vacuum. The error associated with the abundance and the isotopic values is calculated as 1σ. The error associated with the average is obtained by the standard deviation of the four values.

Sample	mass $\cdot 10^{-4}$ g	$^{22}Ne \cdot 10^{-9}$ cm^3 STP / g	$^{21}Ne/^{22}Ne$	Solubility $\cdot 10^{-4}$ cm^3 STP / g · bar
Test6-s1	2.32	9.67 ± 0.04	0.0296 ± 0.0015	3.26
Test6-s2	1.24	10.79 ± 0.04	0.0285 ± 0.0014	3.63
Test6-s3	2.04	8.86 ± 0.02	0.0299 ± 0.0015	2.98
Test6-s4	1.40	8.19 ± 0.02	0.0295 ± 0.0015	2.76
Average		**9.38 ± 1.12**	**0.0294 ± 0.0006**	**3.16 ± 0.38**

Table S-3 ^{22}Ne abundances (in cm^3 STP/g) and ^{20}Ne/^{22}Ne and ^{21}Ne/^{22}Ne ratios measured with the Noblesse 5F-5M mass spectrometer for two neon-bearing glass samples (Test7-s1 and Test7-s2), analysed to check their isotopic composition and homogeneity. The # symbol denotes repeated measurements to test reproducibility, with each measurement corresponding to a new set of aliquots (see Vol 2 in Figure S-1). The glass, free of vesicles, was brought back to liquid state under vacuum for 2 minutes. The error associated with the abundance and the isotopic values is calculated as 1σ. The error associated with the average is obtained by the standard deviation of the test values.

Sample	mass · 10^{-4} g	Number of Aliquots	Blank	measured ^{22}Ne · 10^{-8} cm^3 STP / g	^{20}Ne/^{22}Ne	^{21}Ne/^{22}Ne
Test7-s1 #1	1.18	5	21.07 %	1.22	9.87 ± 0.07	0.0287 ± 0.0010
Test7-s1 #2	1.18	10	14.46 %	1.84	9.78 ± 0.05	0.0290 ± 0.0008
Test7-s1 #3	1.18	10	14.71 %	1.81	9.87 ± 0.05	0.0291 ± 0.0009
				Average	**9.84 ± 0.05**	**0.0289 ± 0.0002**
Test7-s2 #1	2.30	10	5.81 %	2.59	9.82 ± 0.03	0.0288 ± 0.0005
Test7-s2 #2	2.30	10	5.84 %	2.58	9.80 ± 0.03	0.0287 ± 0.0005
				Average	**9.81 ± 0.01**	**0.0287 ± 0.0001**

Table S-4 Measured neon isotopic ratios (corrected for blanks) of the Ne-standard (for the Noblesse 5F-5M mass spectrometer). This set was analysed over ten days, the averages for the two isotopic ratios are represented with the associated 1sigma uncertainties. To correct for mass discrimination, averages of isotopic ratios measured on standards during the same period as for ne-bearing glass were taken as well as an average of 7.02 $\cdot 10^{-15}$ cm^3 STP $\cdot$ cps^{-1} for the sensitivity of ^{22}Ne. The uncertainty of the average represents the standard deviation of the reported set standards.

		Sensitivity $^{22}Ne \cdot 10^{-15}$ (cm^3STP / cps)	**$^{20}Ne/^{22}Ne$**	**$^{21}Ne/^{22}Ne$**
Day 1	STD_1	6.99	10.05 ± 0.02	0.0288 ± 0.0004
	STD_2	7.01	10.04 ± 0.02	0.0300 ± 0.0004
	STD_3	7.03	10.05 ± 0.02	0.0293 ± 0.0003
	STD_4	7.03	10.04 ± 0.02	0.0298 ± 0.0003
	STD_5	7.01	10.03 ± 0.02	0.0300 ± 0.0004
	Average		**10.04 ± 0.01**	**0.0296 ± 0.0005**
Day 2	STD_6	6.96	10.00 ± 0.02	0.0295 ± 0.0003
	STD_7	6.96	10.02 ± 0.02	0.0292 ± 0.0004
	STD_8	6.92	10.00 ± 0.02	0.0298 ± 0.0003
	STD_9	6.88	9.97 ± 0.02	0.0298 ± 0.0003
	STD_10	6.92	10.05 ± 0.02	0.0289 ± 0.0003
	STD_11	6.92	10.05 ± 0.02	0.0295 ± 0.0003
	Average		**10.01 ± 0.03**	**0.0294 ± 0.0003**
Day 3	STD_12	7.20	10.04 ± 0.02	0.0292 ± 0.0004
	STD_13	7.12	10.00 ± 0.02	0.0297 ± 0.0004
	STD_14	7.13	10.05 ± 0.02	0.0294 ± 0.0003
	STD_15	7.11	10.05 ± 0.02	0.0298 ± 0.0004
	STD_16	7.10	10.09 ± 0.02	0.0300 ± 0.0004
	STD_17	7.08	10.04 ± 0.02	0.0294 ± 0.0003
	STD_18	7.00	10.04 ± 0.02	0.0296 ± 0.0004
	mean		**10.04 ± 0.02**	**0.0296 ± 0.0003**
Day 4	STD_19	7.05	10.0 ± 0.02	0.0292 ± 0.0004
	STD_20	7.04	10.03 ± 0.02	0.0298 ± 0.0004
	STD_21	7.03	10.03 ± 0.02	0.0296 ± 0.0003
	STD_22	7.05	10.06 ± 0.02	0.0294 ± 0.0003
	mean		**10.04 ± 0.01**	**0.0295 ± 0.0003**
Day 5	STD_23	6.90	10.04 ± 0.02	0.0294 ± 0.0003
	STD_24	6.96	10.15 ± 0.02	0.0295 ± 0.0003
	STD_25	6.98	10.14 ± 0.02	0.0297 ± 0.0003
	STD_26	7.02	10.14 ± 0.02	0.0296 ± 0.0004
	STD_27	7.06	10.14 ± 0.02	0.0289 ± 0.0004
	STD_28	7.08	10.13 ± 0.02	0.0298 ± 0.0003
	mean		**10.12 ± 0.04**	**0.0295 ± 0.0003**

Table S-5 Experimental conditions. # indicates the experimental run; CO_2, Ne-bearing glass and powder of starting material loaded into the capsule in mg. *P* and *T* are the conditions in the IHPV. $time_{exp}$ is the time at which the experiment was quenched.

Sample	Run	Starting mat. $\cdot 10^{-3}$ g	CO_2 added $\cdot 10^{-3}$ g	Ne-bearing glass $\cdot 10^{-3}$ g	T °C	P_{exp} bar	$time_{exp}$ min
CO_2-bearing glass samples							
ESFa-4	#2	63.20	0.75	-	1200	1598	30
ESFa-8	#3	60.10	0.84	-	1200	1609	240
ESFa-10	#3	58.10	4.49	-	1200	1609	240
ESFa-10E	#7	62.00	0.87	-	1200	1726	1140
ESFa-2D	#7	62.30	3.59	-	1200	1726	1140
ESFa-3D	#8 + 9	55.20	0.38	-	1200	1725	130
ESFa-8D	#10 +11	63.70	2.96	-	1200	1674	360
ESFa-1C	#12	58.90	1.56	-	1200	1671	10
ESFa-2C	#12	56.50	3.10	-	1200	1671	10
ESFa-4C	#13	61.80	0.93	-	1200	1683	60
ESFa-5C	#13	61.80	3.56	-	1200	1683	60
ESFa-6C	#15	58.60	0.41	-	1200	1605	240
ESFa-7C	#15	61.30	4.00	-	1200	1605	240
ESFa-9C	#14	78.20	3.42	-	1200	1660	10
ESFa-10C	#15	61.80	0.81	-	1200	1605	240
ESFa-1B	#14	64.60	0.87	-	1200	1660	10
CO_2+Ne-bearing glass samples							
ESFa-1B	#1	60.70	1.83	6.60	1200	1535	240
ESFa-2B	#1	63.80	0.84	6.50	1200	1535	240
ESFa-3B	#1	51.60	0.84	5.40	1200	1535	240
ESFa-5B	#2	60.40	1.80	6.00	1200	1573	10
ESFa-6B	#2	63.50	3.74	6.30	1200	1573	10
ESFa-7B	#4	63.50	0.90	6.50	1200	1605	240
ESFa-10B	#4	64.10	3.83	6.30	1200	1605	240
ESFa-2A	#4	59.90	0.96	6.30	1200	1605	240
ESFa-5A	#5	62.50	3.65	6.60	1200	1669	10
EN-E3	#7	57.90	0.17	5.90	1200	2015	1800

Table S-6 FTIR data. The average of H_2O and CO_2 concentration was calculated from the number of analytical spots in each sample, the results shown below were calculated using the error propagator developed by the « Digital modelling platform» of ISTO. The thickness belongs to the spot where the analysis was done. Thickness was measured five times at every analysed spot, and the thickness uncertainty corresponds to the standard deviation of these measurements. The density of the silicate liquid, δ_l, was determined using the model of Lange (1994) and Warren (1995). A_{1430} and A_{3525} are the absorbance of the fundamental OH-stretching vibration (~3525 cm^{-1}) and the carbonate doublet (~1430 cm^{-1}) in the mid-infrared (MIR) region.

Sample	Thickness · 10^{-3} cm	δ_L g · l^{-1}	A_{1430}	*sd*	A_{3525}	*sd*	[CO_2] ppm	H_2O wt. %
CO_2-bearing glass								
ESFa-4.3	3.32 ± 0.36	2722 ± 15	0.060	0.002	-	-	722 ± 429	
ESFa-4.4	5.10 ± 0.40	2722 ± 15	0.037	0.003	-	-		
ESFa-8.1	5.58 ± 0.13	2717 ± 7	0.087	0.005	0.063	0.002	893	0.13
ESFa-10.1	4.98 ± 0.18	2734 ± 41	0.114	0.004	0.064	0.003	1022 ± 252	0.10 ± 0.03
ESFa-10.2	6.20 ± 0.21	2734 ± 41	0.088	0.003	0.044	0.002		
ESFa-10.3	5.58 ± 0.13	2734 ± 41	0.095	0.005	0.044	0.003		
ESFa-10E.1	6.06 ± 0.24	2739 ± 4	0.121	0.007	0.239	0.003	1315 ± 169	0.47 ± 0.04
ESFa-10E.4	4.94 ± 0.36	2739 ± 4	0.117	0.004	0.231	0.001		
ESFa-10E.5	4.90 ± 0.25	2739 ± 4	0.136	0.002	0.217	0.002		
ESFa-10E.6	5.52 ± 0.20	2739 ± 4	0.118	0.006	0.217	0.001		
ESFa-2D.1	8.46 ± 0.19	2751 ± 7	0.162	0.006	0.303	0.002	1059 ± 111	0.39 ± 0.04
ESFa-2D.2	8.68 ± 3.40	2751 ± 7	0.144	0.007	0.274	0.002		
ESFa-2D.3	8.58 ± 0.31	2751 ± 7	0.175	0.004	0.336	0.002		
ESFa-3D.1	3.04 ± 0.67	2772 ± 44	0.063	0.002	-	-	925 ± 200	
ESFa-3D.2	5.92 ± 0.47	2772 ± 44	0.085	0.002	-	-		
ESFa-3D.3	5.92 ± 0.47	2772 ± 44	0.086	0.002	-	-		
ESFa-8D.1	9.68 ± 0.11	2735 ± 13	0.111	0.005	-	-	702 ± 114	
ESFa-8D.3	9.16 ± 0.17	2735 ± 13	0.113	0.004	-	-		
ESFa-8D.4	9.40 ± 0.16	2735 ± 13	0.126	0.009	-	-		
ESFa-8D.4.2	9.66 ± 0.11	2735 ± 13	0.117	0.004	-	-		

Sample	Thickness · 10^{-3} cm	δ_L g · l^{-1}	A_{1430}	*sd*	A_{3525}	*sd*	[CO_2] ppm	H_2O wt. %
ESFa-8D.5	10.66 ± 0.38	2735 ± 13	0.164	0.005	-	-		
ESFa-8D.6	9.64 ± 0.18	2735 ± 13	0.090	0.002	-	-		
ESFa-1C.1	5.50 ± 0.24	2762 ± 56	0.086	0.002	-	-	971 ± 159	
ESFa-1C.2	5.36 ± 0.13	2762 ± 56	0.084	0.003	-	-		
ESFa-1C.3	6.68 ± 0.41	2762 ± 56	0.137	0.004	-	-		
ESFa-2C.1	3.68 ± 0.29	2761 ± 31	0.024	0.003	-	-	668 ± 304	
ESFa-2C.2	4.24 ± 0.27	2761 ± 31	0.049	0.003	-	-		
ESFa-2C.3	4.26 ± 0.81	2761 ± 31	0.074	0.006	-	-		
ESFa-4C.2	2.64 ± 0.19	2742 ± 18	0.080	0.005	-	-	1710 ± 3	
ESFa-5C.1	4.96 ± 0.19	2754 ± 32	0.063	0.003	-	-	722	
ESFa-6C.1.1	6.68 ± 0.33	2730 ± 21	0.089	0.005	-	-	700 ± 84	
ESFa-6C.1.2	6.72 ± 0.19	2730 ± 21	0.086	0.004	-	-		
ESFa-6C.2.1	7.00 ± 0.35	2730 ± 21	0.081	0.004	-	-		
ESFa-6C.2.2	7.00 ± 0.35	2730 ± 21	0.071	0.004	-	-		
ESFa-6C.2.3	7.02 ± 0.22	2730 ± 21	0.096	0.006	-	-		
ESFa-7C.1	7.18 ± 0.31	2773 ± 57	0.106	0.006	-	-	915 ± 137	
ESFa-7C.2	5.78 ± 0.36	2773 ± 57	0.088	0.010	-	-		
ESFa-7C.3	5.72 ± 0.19	2773 ± 57	0.109	0.006	-	-		
ESFa-7C.4	5.78 ± 0.36	2773 ± 57	0.108	0.007	-	-		
ESFa-7C.5	7.82 ± 0.22	2773 ± 57	0.107	0.013	-	-		
ESFa-9C.1	5.00 ± 0.21	2762 ± 12	0.064	0.003	0.082	0.004	585 ± 178	0.21 ± 0.04
ESFa-9C.2	4.56 ± 0.55	2762 ± 12	0.026	0.002	0.082	0.002		
ESFa-9C.3	4.56 ± 0.55	2762 ± 12	0.052	0.002	0.081	0.002		
ESFa-9C.4	3.72 ± 0.16	2762 ± 12	0.043	0.003	0.093	0.002		
ESFa-10C.1	5.22 ± 0.26	2731 ± 13	0.078	0.006	-	-	931 ± 97	
ESFa-10C.2	5.22 ± 0.26	2731 ± 13	0.083	0.007	-	-		
ESFa-10C.3	5.40 ± 0.21	2731 ± 13	0.098	0.007	-	-		

Sample	Thickness · 10^{-3} cm	δ_L g · l^{-1}	A_{1430}	*sd*	A_{3525}	*sd*	[CO_2] ppm	H_2O wt. %
ESFa-10C.3	5.40 ± 0.21	2731 ± 13	0.098	0.007	-	-		
ESFa-1B.1	4.40 ± 0.17	2731 ± 13	0.034	0.003	0.099	0.009	707 ± 267	0.24 ± 0.04
ESFa-1B.2	4.92 ± 0.16	2731 ± 13	0.060	0.003	0.124	0.006		
ESFa-1B.3	4.92 ± 0.16	2731 ± 13	0.085	0.004	0.086	0.006		
CO_2+Ne-bearing glass								
ESFa-1B.1	5.00 ± 0.25	2678 ± 46	0.105	0.010			1328 ± 158	
ESFa-1B.2	4.92 ± 0.27	2678 ± 46	0.122	0.006				
ESFa-2B.1	3.52 ± 0.19	2739 ± 75	0.079	0.004			1023 ± 259	
ESFa-2B.2	3.52 ± 0.19	2739 ± 75	0.064	0.006				
ESFa-2B.3	4.08 ± 0.30	2739 ± 75	0.055	0.004				
ESFa-3B.1	8.22 ± 0.11	2691 ± 7	0.099	0.003			721 ± 188	
ESFa-3B.2	8.22 ± 0.11	2691 ± 7	0.108	0.001				
ESFa-3B.3	8.22 ± 0.11	2691 ± 7	0.128	0.002				
ESFa-3B.4	7.32 ± 0.19	2691 ± 7	0.053	0.009				
ESFa-3B.5	5.68 ± 0.28	2691 ± 7	0.082	0.003				
ESFa-5B.1	2.58 ± 0.25	2755 ± 4	0.081	0.004			1705 ± 101	
ESFa-5B.2	2.66 ± 0.22	2755 ± 4	0.077	0.004				
ESFa-6B.1	4.16 ± 0.38	2758 ± 3	0.052	0.002	0.120	0.000	880 ± 240	0.30 ± 0.02
ESFa-6B.2	4.16 ± 0.38	2758 ± 3	0.077	0.001	0.107	0.001		
ESFa-7B.1	3.42 ± 0.22	2728 ± 8	0.090	0.002			1546 ± 66	
ESFa-7B.2	3.40 ± 0.43	2728 ± 8	0.095	0.003				
ESFa-10B.1	3.90 ± 0.22	2707 ± 5	0.087	0.004			1197 ± 119	
ESFa-10B.2	4.18 ± 0.18	2707 ± 5	0.081	0.003				
ESFa-2A.1	6.42 ± 0.20	2715 ± 20	0.120	0.004			1023 ± 63	
ESFa-2A.6	3.28 ± 0.13	2715 ± 20	0.056	0.002				
ESFa-5A.1	3.38 ± 0.84	2770 ± 36	0.064	0.003			1043 ± 47	

Sample	Thickness · 10^{-3} cm	δ_L g · l^{-1}	A_{1430}	*sd*	A_{3525}	*sd*	[CO_2] ppm	H_2O wt. %
ESFa-5A.2	3.40 ± 0.71	2770 ± 36	0.060	0.005				
EN-E3.1	4.76 ± 0.17	2770 ± 6	0.213	0.001	0.4330	0.0019	2385 ± 162	0.91 ± 0.06
EN-E3.2	4.76 ± 0.17	2770 ± 6	0.187	0.003	0.3600	0.0007		
EN-E3.3	4.76 ± 0.17	2770 ± 6	0.189	0.003	0.3932	0.0016		
EN-E3.4	4.76 ± 0.17	2770 ± 6	0.205	0.004	0.3864	0.0009		
EN-E3.5	4.76 ± 0.17	2770 ± 6	0.217	0.004	0.4038	0.0013		

Table S-7 Measured neon isotopic ratios (corrected for blanks) of the Ne-standard (for the Helix-SDT mass spectrometer). This set was analysed over sixteen months, the averages for the two isotopic ratios are represented with the associated 1sigma uncertainties. To correct for mass discrimination, averages of isotopic ratios and sensitivity measured on standards during the same period as for vesicles (Table S-8) were taken. The uncertainty of the average represents the standard deviation of the reported set standards.

	Sensitivity $^{22}Ne \cdot 10^{-15}$ (cm^3STP / cps)	$^{20}Ne/^{22}Ne$	$^{21}Ne/^{22}Ne$
STD_1	3.65	10.04 ± 0.02	0.0291 ± 0.0003
STD_2	3.69	10.30 ± 0.04	0.0289 ± 0.0002
STD_3	3.70	10.23 ± 0.03	0.0292 ± 0.0003
STD_4	3.67	10.20 ± 0.02	0.0290 ± 0.0001
STD_5	2.43	10.22 ± 0.03	0.0291 ± 0.0003
STD_6	3.78	10.34 ± 0.03	0.0287 ± 0.0002
STD_7	3.69	10.31 ± 0.03	0.0292 ± 0.0002
STD_8	3.70	10.23 ± 0.02	0.0288 ± 0.0002
STD_9	3.72	10.32 ± 0.04	0.0285 ± 0.0002
STD_10	3.68	10.27 ± 0.03	0.0294 ± 0.0002
STD_11	3.67	10.26 ± 0.03	0.0288 ± 0.0002
STD_12	3.61	10.20 ± 0.03	0.0290 ± 0.0003
STD_13	3.64	10.24 ± 0.02	0.0290 ± 0.0003
STD_14	3.73	10.27 ± 0.03	0.0283 ± 0.0003
STD_15	3.76	10.22 ± 0.03	0.0288 ± 0.0003
STD_16	3.73	10.18 ± 0.02	0.0286 ± 0.0002
STD_17	3.65	10.28 ± 0.03	0.0288 ± 0.0003
mean		**10.24 ± 0.07**	**0.0289 ± 0.0003**
STD_18	3.66	10.13 ± 0.03	0.0290 ± 0.0003
STD_19	3.64	10.02 ± 0.04	0.0287 ± 0.0002
STD_20	3.69	10.27 ± 0.03	0.0288 ± 0.0003
STD_21	3.74	10.38 ± 0.03	0.0288 ± 0.0003
STD_22	3.69	10.20 ± 0.03	0.0288 ± 0.0003
STD_23	3.68	10.29 ± 0.03	0.0288 ± 0.0003
STD_24	3.67	10.32 ± 0.04	0.0293 ± 0.0004
STD_25	3.68	10.32 ± 0.04	0.0284 ± 0.0003
STD_26	3.64	9.92 ± 0.03	0.0286 ± 0.0003
STD_27	3.65	10.03 ± 0.04	0.0286 ± 0.0002
STD_28	3.66	10.07 ± 0.04	0.0289 ± 0.0004
STD_29	3.66	10.15 ± 0.03	0.0286 ± 0.0002
STD_30	3.66	10.21 ± 0.02	0.0289 ± 0.0002
STD_31	3.71	10.09 ± 0.04	0.0293 ± 0.0003
STD_32	3.70	10.24 ± 0.04	0.0291 ± 0.0003
STD_33	3.72	10.19 ± 0.02	0.0292 ± 0.0004
mean		**10.18 ± 0.13**	**0.0289 ± 0.0003**

Table S-8 Measured ^{22}Ne abundances and Ne isotopic compositions obtained with the HELIX-SFT mass spectrometer of the vesicles for the experimental samples *ESFa-3B-204min*, *ESFa-5B-10min* and *ESFa-6B-10min*. Errors are 1 sigma uncertainties. Pb_{Tot} is the partial pressure resulting from vesicle gas expansion to the purification line when piercing. *Air* composition from (Ozima and Podosek, 2002). **The gas extracted in these vesicles corresponds to three vesicles pierced at the same time.

Sample	$Pb_{Tot} \cdot 10^{-7}$ bar	$^{22}Ne \cdot 10^{-12}$ cm^3 STP	$^{20}Ne/^{22}Ne$	$^{21}Ne/^{22}Ne$
ESFa-3B vesicles (240 min)				
V1	40	5.00 ± 0.10	9.97 ± 0.06	0.0288 ± 0.0006
V2**	79	6.36 ± 0.12	10.28 ± 0.05	0.0303 ± 0.0006
V3	26	3.33 ± 0.06	9.97 ± 0.09	0.0303 ± 0.0007
V4	22	4.00 ± 0.08	9.8 ± 0.06	0.0285 ± 0.0007
V5	165	18.25 ± 0.35	10.05 ± 0.05	0.0296 ± 0.0005
V6	14	2.51 ± 0.05	9.75 ± 0.08	0.0286 ± 0.0007
V7	11	1.93 ± 0.04	9.85 ± 0.12	0.0282 ± 0.0007
V1 ALA	19	2.08 ± 0.04	9.82 ± 0.08	0.0307 ± 0.0007
V2 ALA	15	2.51 ± 0.05	10.50 ± 0.13	0.0303 ± 0.0005
V3 ALA	350	3.84 ± 0.07	10.26 ± 0.10	0.0298 ± 0.0004
V4 ALA	9	1.73 ± 0.03	9.84 ± 0.08	0.0294 ± 0.0007
V5 ALA	11	1.67 ± 0.02	9.88 ± 0.10	0.0304 ± 0.0009
V6 ALA	9	1.20 ± 0.02	10.08 ± 0.11	0.0282 ± 0.0010
V7 ALA	6	0.98 ± 0.02	10.06 ± 0.09	0.0291 ± 0.0007
V8 ALA	13	2.04 ± 0.04	10.03 ± 0.10	0.0292 ± 0.0008
V9 ALA**	36	4.54 ± 0.09	9.73 ± 0.08	0.0292 ± 0.0005
V10 ALA	35	5.89 ± 0.11	9.76 ± 0.07	0.0288 ± 0.0004
V11 ALA	21	2.59 ± 0.05	9.77 ± 0.09	0.0287 ± 0.0007
ESFa-5B vesicles (10 min)				
V1	173	23.25 ± 0.26	9.97 ± 0.02	0.0289 ± 0.0002
V2	19	2.95 ± 0.03	10.03 ± 0.04	0.0289 ± 0.0004
V3	28	3.89 ± 0.04	9.96 ± 0.04	0.0290 ± 0.0005
V4	18	2.62 ± 0.03	10.24 ± 0.05	0.0302 ± 0.0005
V5	19	2.34 ± 0.03	10.02 ± 0.05	0.0284 ± 0.0005
V6	28	3.57 ± 0.04	9.80 ± 0.03	0.0284 ± 0.0004
V7	178	24.24 ± 0.27	9.81 ± 0.02	0.0293 ± 0.0001
V10	20	2.99 ± 0.03	9.62 ± 0.04	0.0283 ± 0.0003
V11	31	4.60 ± 0.05	9.44 ± 0.04	0.0296 ± 0.0002
V12	23	3.62 ± 0.04	9.73 ± 0.05	0.0300 ± 0.0005
ESFa-6B vesicles (10 min)				
V1	9	1.45 ± 0.01	9.40 ± 0.08	0.0264 ± 0.0009
V2	49	5.01 ± 0.05	9.56 ± 0.03	0.0297 ± 0.0005
V3	9	1.49 ± 0.01	9.58 ± 0.07	0.0289 ± 0.0008
Air			9.8	0.0290
MFF_{Ne}			10.28	0.0297

Table S-9 Vesicle size distribution parameters of the experimental samples analysed by microtomography. The image treatment was done by using *ImageJ*. *Nb* represents the number of counted bubbles in one slice of the image stack obtained by the tomography; *Area* is the analysed surface of the glass; Bubble density corresponds to the number of vesicles by surface area; D_{max} and D_{mean} correspond to the maximum and mean diameter of the vesicles of the scanned slice; *Ln(n)* is the density of the population of vesicles obtained by the linear regression of *Ln(n)* vs D_{max}; *a* is the slope of the trend line; R^2 is the correlation coefficient of the trend line; $D_{mean.th}$ is the theoretical mean diameter obtained by the inverse of the slope (-1/a); *Ves.* is the obtained vesicularity by VGSudioMax.

Sample	Nb	Area (mm^2)	Bubbles density (mm^{-2})	D_{max} (µm)	D_{mean} (µm)	Ln(n) (mm^{-4})	a (mm^{-1})	R^2	$D_{mean.th.}$ (-1/a) (µm)	Ves (%)
CO_2-bearing glass										
ESFa-4	376	9.0	41.9	99.9	19.8	12.5 ± 0.3	-66.9 ± 5.8	0.9	15.0	0.9
ESFa-8	145	4.8	30.1	118.8	19.5	12.0 ± 0.4	-63.7 ± 7.8	0.9	15.7	0.5
ESFa-10	196	12.1	16.2	108.3	21.3	11.3 ± 0.4	-62.9 ± 7.7	0.9	15.9	0.6
ESFa-10E	497	12.8	38.7	102.8	20.1	12.3 ± 0.3	-63.6 ± 6.8	0.9	15.7	0.7
ESFa-2D	64	2.9	21.8	179.7	33.1	10.3 ± 0.6	-36.4 ± 7.2	0.7	27.4	0.8
ESFa-3D	555	11.4	48.6	140.0	23.1	12.3 ± 0.2	-56.1 ± 3.7	1.0	17.8	0.9
ESFa-8D	209	13.4	15.6	229.7	24.9	10.7 ± 0.4	-46.0 ± 3.8	0.9	21.7	1.4
ESFa-1C	583	10.4	56.1	322.3	28.0	10.9 ± 0.5	-30.2 ± 3.4	0.9	33.1	4.2
ESFa-2C	400	11.8	33.8	140.4	22.0	12.4 ± 0.5	-63.2 ± 6.1	0.9	15.8	0.2
ESFa-4C	332	5.2	64.5	144.0	18.2	13.4 ± 0.5	-80.6 ± 8.0	0.9	12.4	2.0
ESFa-5C	490	12.0	40.8	159.4	24.4	11.8 ± 0.4	-49.5 ± 5.3	0.9	20.2	1.6
ESFa-6C	451	12.9	35.0	163.5	15.5	12.4 ± 0.4	-73.7 ± 5.7	0.9	13.6	0.5
ESFa-7C	223	9.8	22.8	158.1	23.3	11.3 ± 0.5	-52.3 ± 6.9	0.9	19.1	1.1
ESFa-9C	257	4.9	52.0	168.5	26.4	11.9 ± 0.5	-45.7 ± 5.9	0.9	21.9	3.1
ESFa-10C	524	16.1	32.6	159.2	24.9	11.8 ± 0.3	-52.5 ± 4.0	0.9	19.0	2.2
ESFa-1B	732	12.8	57.3	170.1	20.3	12.9 ± 0.5	-67.4 ± 5.9	0.9	14.8	2.0
CO_2+Ne-bearing glass										
ESFa-1B	384	9.5	40.5	119.8	18.0	12.6 ± 0.3	-70.1 ± 4.9	1.0	14.3	1.5
ESFa-2B	1111	13.9	80.2	191.1	16.6	13.5 ± 0.4	-77.1 ± 5.0	1.0	13.0	1.2

Sample	Nb	Area (mm^2)	Bubbles density (mm^{-2})	D_{max} (µm)	D_{mean} (µm)	Ln(n) (mm^{-4})	a (mm^{-1})	R^2	$D_{mean.th.}$ (-1/a) (µm)	Ves (%)
ESFa-3B	953	10.6	89.7	161.8	18.5	12.9 ± .5	-60.3 ± 7.0	0.9	16.6	1.7
ESFa-5B	133	11.3	11.8	196.6	37.9	9.5 ± 0.6	-32.0 ± 6.2	0.7	31.3	0.9
ESFa-6B	39	5.6	6.9	90.6	29.5	10.1 ± 1.4	-51.7 ± 11.6	0.7	19.4	0.4
ESFa-7B	494	13.3	37.1	166.2	22.6	11.6 ± 0.4	-47.8 ± 5.5	0.9	20.9	4.0
ESFa-10B	157	4.7	33.3	91.4	19.8	12.1 ± 0.3	-63.4 ± 7.2	0.9	15.8	0.8
ESFa-2A	702	10.3	68.0	160.9	17.3	12.5 ± 0.5	-56.7 ± 5.9	0.9	17.6	0.5
ESFa-5A	308	8.1	37.9	273.7	30.3	10.5 ± 0.7	-31.1 ± 5.2	0.8	32.1	2.5
EN-E3	-	-	-	-	-	-	-	-	-	-

Table S-10 CO_2 diffusion in the melt (D_{CO2}), bubble displacement (B_d) and bubble growth (G_r) at the time at which the experiments were quenched.

Sample	$time_{exp}$ min	D_{CO2} (cm)	B_d (cm)	G_r (cm)
CO_2-bearing glass				
ESFa-4	30	1.3E-02	2.5E-03	2.5E-05
ESFa-8	240	3.6E-02	3.1E-02	2.1E-04
ESFa-10	240	3.6E-02	3.7E-02	2.1E-04
ESFa-10E	1140	7.9E-02	2.9E-01	1.0E-03
ESFa-2D	1140	7.9E-02	7.1E-01	1.7E-03
ESFa-3D	130	2.7E-02	1.5E-02	1.3E-04
ESFa-8D	360	4.4E-02	4.8E-02	4.3E-04
ESFa-1C	10	7.4E-03	1.7E-03	1.8E-05
ESFa-2C	10	7.4E-03	1.0E-03	8.8E-06
ESFa-4C	60	1.8E-02	4.2E-03	4.1E-05
ESFa-5C	60	1.8E-02	7.7E-03	6.7E-05
ESFa-6C	240	3.6E-02	1.2E-02	1.8E-04
ESFa-7C	240	3.6E-02	2.8E-02	2.5E-04
ESFa-9C	10	7.4E-03	2.9E-03	1.2E-05
ESFa-10C	240	3.6E-02	3.2E-02	2.5E-04
ESFa-1B	10	7.4E-03	1.8E-03	8.2E-06
CO_2+Ne-bearing glass				
ESFa-1B	240	3.7E-02	1.6E-02	1.9E-04
ESFa-2B	240	3.7E-02	1.4E-02	1.7E-04
ESFa-3B	240	3.7E-02	1.7E-02	2.2E-04
ESFa-5B	10	7.5E-03	3.1E-03	1.7E-05
ESFa-6B	10	7.5E-03	4.3E-03	1.1E-05
ESFa-7B	240	3.6E-02	2.6E-02	2.8E-04
ESFa-10B	240	3.6E-02	2.0E-02	2.1E-04
ESFa-2A	240	3.6E-02	1.5E-02	2.4E-04
ESFa-5A	10	7.4E-03	2.0E-03	1.8E-05
EN-E3	1800	9.9E-02	-	-

Supplementary Figures

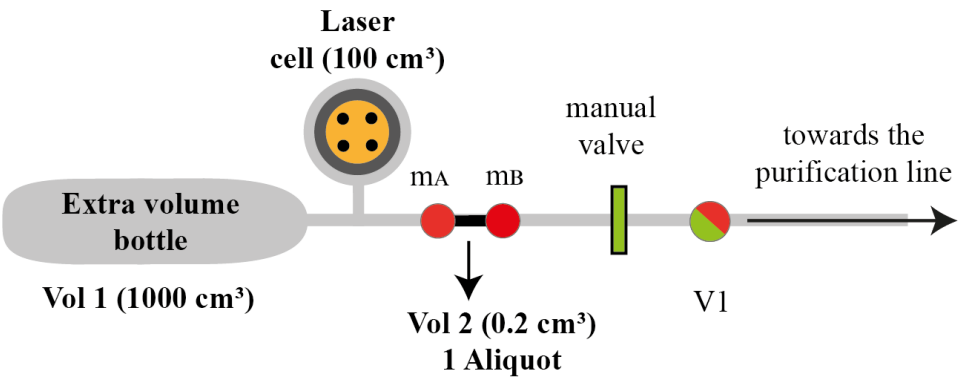

Figure S-1 Extraction and under-vacuum expansion volume attached to the purification line of the Noblesse mass spectrometer type (not at scale). The automatic valve, V1, is controlled by LabVIEW ©. The red circles show the manual valves for controlling Vol 2; the green rectangle valve isolates the expansion volume line from the purification line and V1, representing the automatic valve leading to the purification line. The extra volume bottle represents Vol 1 (1000 cm^3). The laser cell holds the chunk of glass to be analysed and consists of a volume of 100 cm^3 (Vol 3).

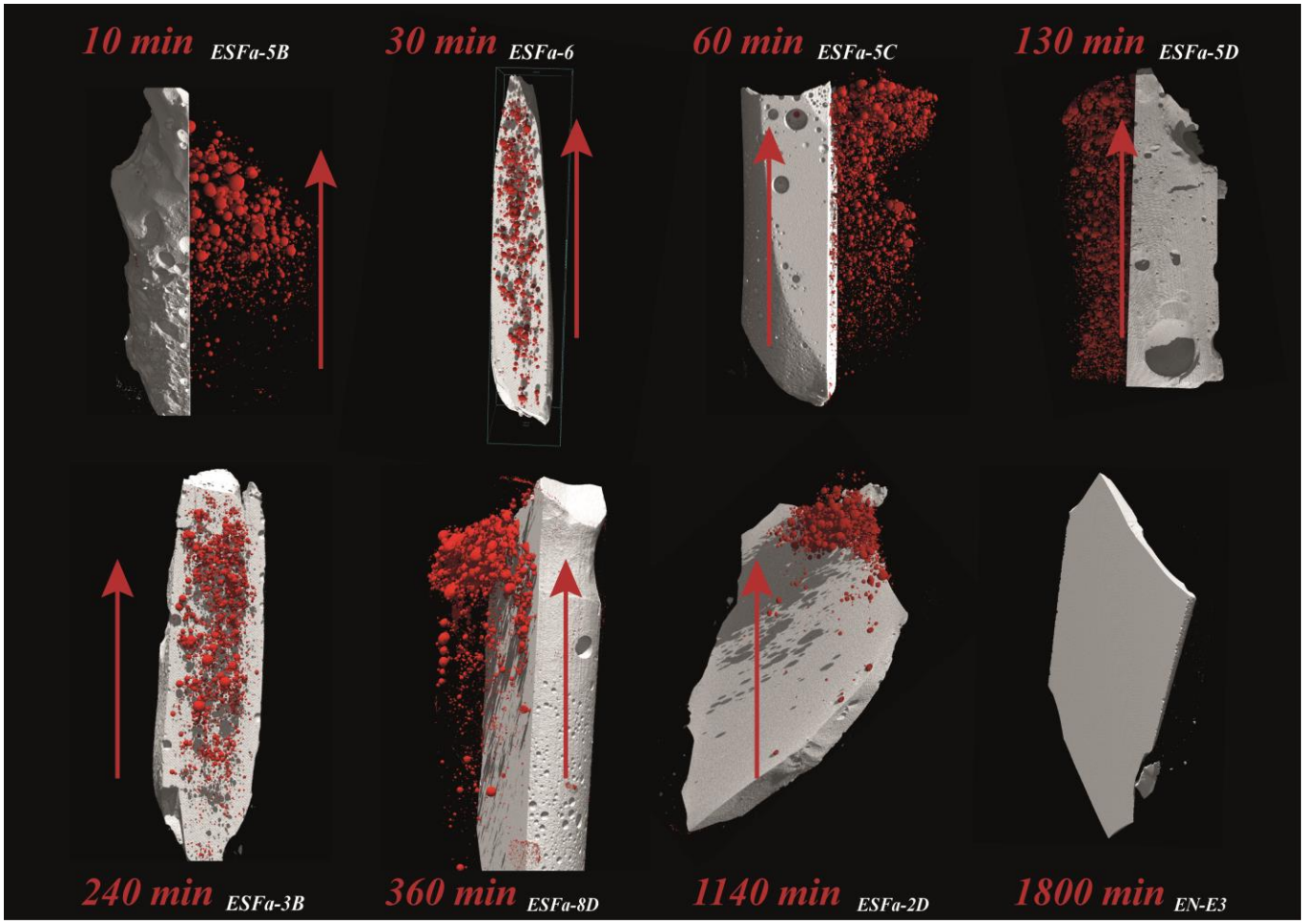

Figure S-2 3D Representative images for every experimental time. The experiment time increases from 10 to 1800 minutes, from top to bottom of the image. The accumulation of vesicles at one of the limits of the sample is evident when the experimental time increases until there are no more vesicles (at 1800 min of the experiment). The length of samples ranges from 1 to 1.2 cm. The red line marks the direction of bubble flow towards the top of the capsule.

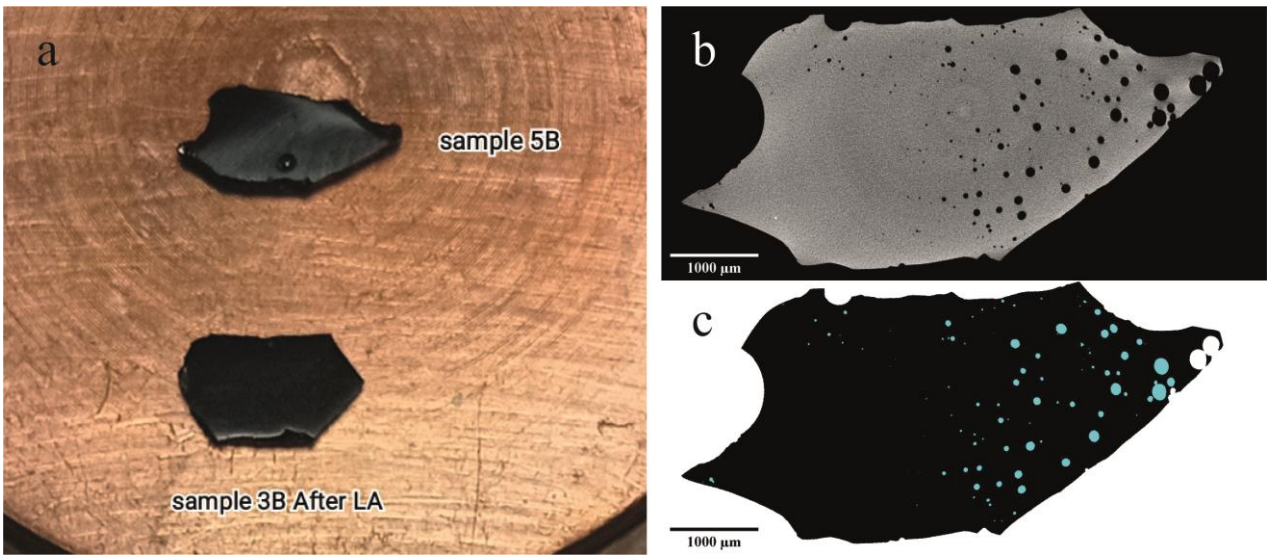

Figure S-3 (a) *ESFa-3B-240min* (approximately 5 mm in length) and *ESFa-5B-10min* samples (approximately 7 mm in length) placed inside the laser cell. The images on the right display the *ESFa-5B-10min* sample, with the image obtained through tomography **(b)** and further processed using *ImageJ* **(c)** to determine the vesicle size distribution.

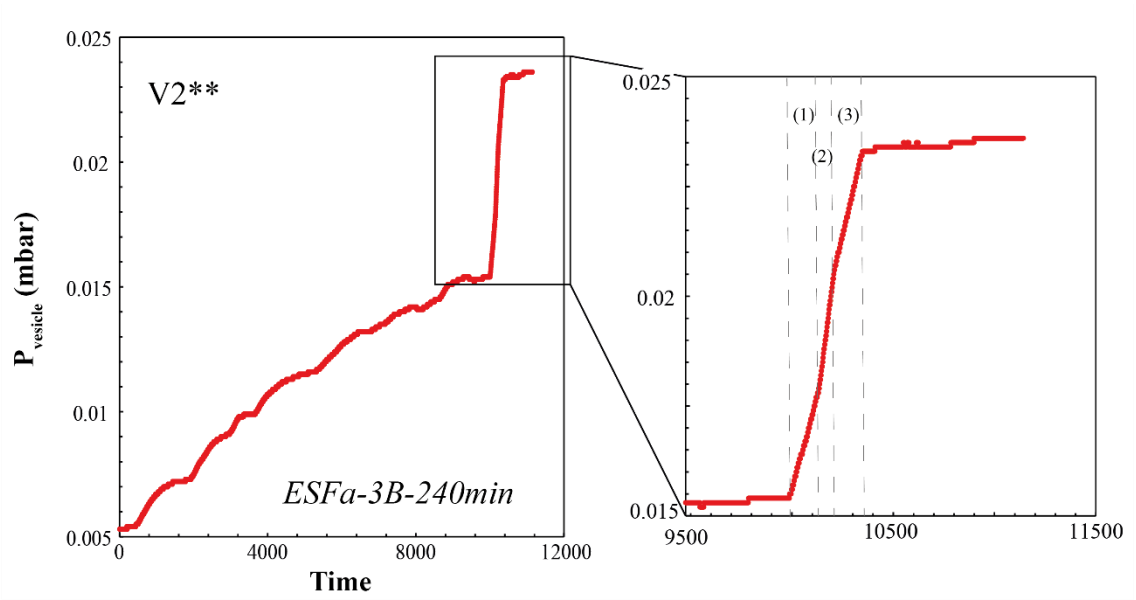

Figure S-4 Partial pressure in mbar, as recorded by the manometer, during laser ablation of three vesicles from sample *ESFa-3B-240min*. The blow-up on the right reveals three changes in the slope of the pressure curve. Dashed lines mark the representative pressure for each pierced vesicle, labelled (1), (2), and (3) in the right-hand plot. The time is not represented in specific units but is instead recorded by the software.

Supplementary Information References

Behrens, H., Zhang, Y. (2001) Ar diffusion in hydrous silicic melts: implications for volatile diffusion mechanisms and fractionation. *Earth Planetary Science Letters* 192, 363–376. https://doi.org/10.1016/S0012-821X(01)00458-7

Bottinga, Y., Richet, P., (1981) High pressure and temperature equation of state and calculation of the thermodynamic properties of gaseous carbon dioxide. *American Journal of Sc*ience 281, 615–660. https://doi.org/10.2475/ajs.281.5.615

Di Carlo, I., Pichavant, M., Rotolo, S.G., Scaillet, B. (2006) Experimental crystallization of a high-K arc basalt: the golden pumice, Stromboli volcano (Italy). *Journal of Petrol*ogy 47, 1317–1343. https://doi.org/10.1093/petrology/egl011

Giordano, D., Russell, J.K., Dingwell, D.B. (2008) Viscosity of magmatic liquids: a model. *Earth Planetary Science Lett*ers 271, 123–134. https://doi.org/10.1016/j.epsl.2008.03.038

Jambon, A., Weber, H., Braun, O. (1986) Solubility of He, Ne, Ar, Kr and Xe in a basalt melt in the range 1250–1600 C. Geochemical implications. *Geochimica Cosmochimica Acta* 50, 401–408. https://doi.org/10.1016/0016-7037(86)90193-6

Jiménez-Mejías, M., Andújar, J., Scaillet, B., Casillas, R. (2021) Experimental determination of H_2O and CO_2 solubilities of mafic alkaline magmas from Canary Islands. *Comptes Rendus Géoscience* 353, 289–314. https://10.5802/crgeos.84

Lange, R.A. (1994) Volatiles in Magmas. In: Carroll, M.R., Holloway, J.R. (Eds.). *De Gruyter, pp*. 331–370. https://doi.org/10.1515/9781501509674-015

Nowak, M., Schreen, D., Spickenbom, K. (2004) Argon and CO_2 on the race track in silicate melts: a tool for the development of a CO2 speciation and diffusion model. *Geochimica Cosmochimica Acta* 68, 5127–5138. https://doi.org/10.1016/j.gca.2004.06.002

Ozima, M., Podosek, F.A. (2002) Noble gas geochemistry. *Cambridge University Press*. https://doi.org/10.1017/CBO9780511545986

Sarda, P., Graham, D. (1990) Mid-ocean ridge popping rocks: implications for degassing at ridge crests. *Earth and Planetary Science Letters* 97, 268–289. https://doi.org/10.1016/0012-821X(90)90047-2

Stolper E. (1982) The speciation of water in silicate melts. *Geochimica Cosmochimica Acta* 46:2609–2620. https://doi.org/10.1016/0016-7037(82)90381-7.

Stout, V.L., Gibbons, M.D. (1955) Gettering of gas by titanium. *Journal of Applied Phys*ics 26, 1488–1492. https://doi.org/10.1063/1.1721936

Warren, P.H. (1995) Extrapolated partial molar densities of SO_3, P_2O_5, and other oxides in silicate melts. *American Mineral*ogist 80, 1085–1088. https://doi.org/10.2138/am-1995-9-1029

Watson, E.B., Sneeringer, M.A., Ross, A. (1982) Diffusion of dissolved carbonate in magmas: experimental results and applications. *Earth and Planetary Science Lett*ers 61, 346–358. https://doi.org/10.1016/0012-821X(82)90065-6

Zhang, Y., Xu, Z. (1995) Atomic radii of noble gas elements in condensed phases. *American Mineralogist* 80, 670–675. https://doi.org/10.2138/am-1995-7-803

Zhang, Y., Xu, Z., Zhu, M., Wang, H. (2007) Silicate melt properties and volcanic eruptions. *Reviews in Geophysics* 45. https://doi.org/10.1029/2006RG000216

« Digital modelling platform» https://calcul-isto.cnrs-orleans.fr/apps/propagator/